

**Aerosol physicochemical properties and implications ~~of~~ visibility during an intense haze episode during winter in Beijing**

Y. H. Wang<sup>1,2</sup>, Z. R. Liu<sup>1</sup>, J. K. Zhang<sup>1</sup>, B. Hu<sup>1</sup>, D. S. Ji<sup>1</sup>, Y. C. Yu<sup>1</sup> and Y. S. Wang<sup>1,2</sup>

1 State Key Laboratory of Atmospheric Boundary Layer Physics and Atmospheric

Chemistry (LAPC), Institute of Atmospheric Physics, Chinese Academy of Sciences,

Beijing 100029, China

2 College of Atmospheric Sciences, Lanzhou University, Lanzhou, 730000, China

\*Corresponding Author: Y. S. Wang

Email: [wys@mail.iap.ac.cn](mailto:wys@mail.iap.ac.cn)

## 1 Abstract

2 The evolution of physical, chemical and optical properties of urban aerosol particles  
3 was characterized during an extremely haze episode in Beijing, PRC, from January 24  
4 through January 31, 2013 based on in-situ measurements. The average mass  
5 concentrations of  $PM_1$  (~~particle aerodynamic diameter no more than 1 micrometer~~),  
6  $PM_{2.5}$  (~~particle aerodynamic diameter no more than 1 micrometer~~) and  $PM_{10}$  (~~particle  
76 aerodynamic diameter no more than 1 micrometer~~) were  $99 \pm 67 \mu\text{g}\cdot\text{m}^{-3}$  (average  $\pm$   
87 stdev),  $188 \pm 128 \mu\text{g}\cdot\text{m}^{-3}$  and  $265 \pm 157 \mu\text{g}\cdot\text{m}^{-3}$ , respectively. A significant increase in  
98  $PM_{1-2.5}$  fraction was observed during the most heavily polluted period. The average  
109 scattering coefficient at 550 nm was  $877 \text{ Mm}^{-1} \pm 624 \text{ Mm}^{-1}$ . An increasing relative  
110 amount of coarse particles can be deduced from the variations of backscattering ratios,  
111 asymmetry parameter and scattering Ångström exponent. Particle number size  
112 distributions between 14 nm-2500 nm diameter showed high number concentrations,  
113 particularly in the nucleation mode and accumulation mode. Size-resolved chemical  
114 composition of submicron aerosol from a High Resolution-ToF-Aerosol Mass  
115 Spectrometer showed that the mass concentrations of organic, sulfate, nitrate,  
116 ammonium and chlorine mainly resided on 500nm to 800nm (vacuum diameter)  
117 particles, and nitrate and ammonium contributed greatly to particle growth during the  
118 heavily polluted day (January 28).  
119 Increasing relative humidity and stable synoptic conditions on January 28 combined  
120 with heavy pollution on 28 January, lead to enhanced water uptake by the hygroscopic  
121 submicron particles and formation of secondary aerosol, which might be the main

2322 reasons for the severity of the haze episode. Light scattering apportionment showed  
2423 that organic, sulfate, ammonium nitrate and ammonium chloride compounds  
2524 contributed to light scattering fractions of 54%, 24%, 12% and 10%, respectively.  
2625 This study indicated that the organic component in submicron aerosol played an  
2726 important role in visibility degradation during the haze episode in Beijing.

## 2827 **1. Introduction**

2928 Atmospheric aerosol particles play a significant role in radiation balance and climate  
3029 forcing through direct scattering and absorption of solar radiation (Anderson et al.,  
3130 2003; Poschl, 2005; Ramanathan et al., 2001). In addition, they can act as cloud  
3231 condensation nuclei (CCN) and thereby change the cloud albedo and lifetime (Twomey,  
3332 1977). Accordingly, the radiative properties of clouds are indirectly influenced by  
3433 aerosol (Kaufman et al., 2005; Koren et al., 2005; Lohmann and Feichter, 2005).  
3534 Furthermore, the general public has to pay special attention to atmospheric aerosol due  
3635 to its deleterious effect on human health and degradation of visibility (Nel, 2005;  
3736 Watson, 2002), which are closely related to the chemical components, morphology,  
3837 mixing state, size distribution and hygroscopic properties of aerosol particles.  
3938 Along with the rapid economic growth in China, its capital city Beijing has suffered  
4039 substantially from air quality deterioration and visibility degradation, though the mass  
4140 concentration of PM<sub>10</sub> has decreased in Beijing in the last ten years (Liu et al., 2015).  
4241 Accompanied by frequent fog-haze days, the visibility in Beijing has decreased  
4342 dramatically to an unacceptable level. The frequency of visibility between 2km and

4443 10km has increased from 37% in 1999 to 43% in 2007. (Zhang et al., 2010; Zhang et  
4544 al., 2012). The mass loading of fine aerosol particles and their precursors ( e.g. NH<sub>3</sub>,  
4645 volatile organic compounds (VOCs), SO<sub>2</sub> and NO<sub>x</sub>), can accumulate to high levels  
4746 within the planetary boundary layer , especially during periods of persistent synoptic scale  
stagnation  
4847 and strong temperature inversions (Zhang et al., 2013). In the past decade, many  
4948 researches-research projects have been done to characterize the chemical and physical  
properties of  
5049 aerosol particles in Beijing and its surrounding regions. These studies mainly focused  
5150 on the following aspects:

5251 i) Chemical composition, evaluation and sources apportionment based on filter  
5352 sampling and Aerosol Mass Spectrometry (AMS) (Huang et al., 2010b; Sun et  
54 al., 2006; Zhang et al., 2014) .

55 ii) Mass concentration and optical properties of aerosol particles using in-situ  
56 measurements or combined with MODIS (Moderate Resolution Imaging  
57 Spectroradiometer) satellite remote sensing optical depth products (He et al.,  
58 2009; Huang et al., 2010a; Li et al., 2010; Qu et al., 2010; Wang et al., 2012a;  
59 Yang et al., 2009).

60 iii) Aerosol hygroscopic properties, number size distributions, mixing state and  
61 implications for CCN activity, visibility, new particle formation, air pollution  
62 and radiative forcing (Chen et al., 2012; Cheng et al., 2012; Deng et al., 2013;  
63 Liu et al., 2013; Ma et al., 2012; Meier et al., 2009; Pan et al., 2009; Quan et al.,  
64 2011; Wehner et al., 2008; Wu et al., 2007; Zhang et al., 2011; Zhang et al.,

| 65 2010).

66 The above mentioned studies, based on either long-term or short-term observations  
67 provide us with comprehensive knowledge of aerosol properties on days with near  
68 average aerosol concentration levels. However, only a few studies were carried out  
69 ~~under-on~~ highly polluted days, and these studies mainly focus on variations of chemical  
70 composition with the evaluation of synoptic conditions and planetary boundary layer  
71 dynamics. (Huang et al., 2010a; Wang et al., 2012b; Zhao et al., 2013). The interaction  
72 between chemical and physical properties of aerosols was seldom investigated during  
73 haze episodes. Therefore, comprehensive studies of physical, optical and chemical  
74 properties using high resolution measurements are necessary for a better knowledge of  
75 aerosol evolution processes and related visibility degradation during pollution episodes  
76 in Beijing.

77 An intense pollution episode occurred in central and eastern China from January 24  
78 through 31, 2013. The hourly average  $PM_{10}$  exceeded  $600 \mu\text{g}\cdot\text{m}^{-3}$  and non-refractory  
79 submicron particle (NR- $PM_1$ ) exceeded  $400 \mu\text{g}\cdot\text{m}^{-3}$  (Wang et al., 2013), which was the  
80 most extreme haze episode in Beijing in the last decades as far as we know. In this  
81 study, we investigated the evolution of physical, chemical, and optical properties of  
82 urban aerosol particle during the haze episode by using the in-situ measurements.

## 83 **2. Methodology**

### 84 **2.1 Site information and instrumentation**

85 The aerosol sampling site was situated on the roof ( about 15m height above the  
86 surface) of a laboratory building in the yard of the Institute of Atmospheric Physics

87 (IAP), Chinese Academy of Sciences, which was located between the 3<sup>rd</sup> and 4<sup>th</sup> ring  
88 roads of northeast Beijing (Zhang et al., 2014).

89 An integrating nephelometer (Model 3563, TSI inc., Minnesota, USA) was used to  
90 measure the total light scattering and hemispheric back scattering coefficients (for  
91 angles ~~between of~~  $\sim 7^\circ$  ~~to~~  $170^\circ$  ~~and~~  $90^\circ$  ~~to~~  $170^\circ$ , respectively) of low RH aerosol at  
wavelengths of 450, 550  
92 and 700nm, no size-selective inlets were used. The nephelometer was operated at 5L  
93  $\text{min}^{-1}$  with data resolution of one minute. ~~The A~~ calibration was conducted every month  
94 with filtered air and  $\text{CO}_2$  as prescribed by the manufacturer. Subsequently, the data  
95 were corrected for truncation errors and the non-lambertian light source based on the  
96 measured Ångström exponents (Anderson and Ogren, 1998). On average, the corrected  
97 values were within 10% of the measured values. The mass concentration of  $\text{PM}_{10}$  and  
98  $\text{PM}_{2.5}$  were measured by a Thermo TEOM 1400AB/8500 FDMS (Filter Dynamic  
99 Measurement System). The mass concentration of  $\text{PM}_1$  was determined using a  
100 Thermo TEOM 1400.

101 The particle number-size distribution between 14nm and 2500nm diameter was  
102 measured by a Scanning Mobility Particle Sizer (SMPS, TSI inc., Minnesota, USA),  
103 comprising of a model TSI 3080 electrostatic classifier and a model TSI 3775  
104 condensation particle counter (CPC), and an Aerodynamic Particle Sizer (APS, Model  
105 3321, TSI inc., Minnesota, USA). The SMPS data covered the particle size range from  
106 14nm to 533nm, and the APS covered from 542 nm to 2500nm. The size-dependent  
107 diffusional and gravitational losses for the inlet line have been corrected by using the  
108 empirical functions given by Willeke and Baron (1993). The data collected from these

109 two instruments were merged into one particle size spectrum matrix ( 14nm to 2500nm)  
110 according to the methods of Liu et al. (2014) and Beddows et al. (2010).

111 The aerosol chemical composition was acquired using an Aerodyne High-Resolution  
112 Time-of-Flight Aerosol Mass Spectrometer (HR-ToF-AMS, or AMS, Aerodyne  
113 Research Inc., Billerica, MA, USA). The organic matter, sulfate, nitrate, ammonium  
114 and chlorine in non-refractory submicron particle mass-size distributions (NR-PM<sub>1</sub>)  
115 were determined under V and W ion optical modes alternatively every 7.5 minutes.

116 Detailed information of data analysis, collection efficiency (CE) and relative ionization  
117 efficiency of the instrument were introduced by Zhang et al. (2014). Simultaneously,  
118 the gaseous pollutants (e.g., NO, NO<sub>x</sub>, CO, O<sub>3</sub> and SO<sub>2</sub>) were measured using Thermo  
119 instruments (series of 42i, 48i, 49i and 43i, respectively, Thermo Fisher Scientific,  
120 Franklin, Massachusetts, USA). Detailed introduction and calibrations were given by  
121 (Tang et al., 2012; Wang et al., 2014).

122 An automatic meteorological observation instrument (Milos520, Vaisala, Finland) was  
123 used to obtain meteorological parameters (relative humidity, air temperature, wind  
124 speed and direction). The time base for all data in the study was Beijing zone time  
125 (UTC+8).

### 126 **3. Results and discussion**

#### 127 **3.1 Aerosol mass concentration and meteorological parameters**

128 Figure 1 shows the mass concentrations of PM<sub>1</sub>, PM<sub>1-2.5</sub>, PM<sub>2.5-10</sub> and mass  
129 concentration ratios of PM<sub>1</sub>/PM<sub>2.5</sub>, PM<sub>2.5</sub>/PM<sub>10</sub> during the period. The average mass



130 concentrations of  $PM_1$ ,  $PM_{2.5}$  and  $PM_{10}$  are  $99.1 \pm 67.1 \mu\text{g}\cdot\text{m}^{-3}$ ,  $188.3 \pm 128.8 \mu\text{g}\cdot\text{m}^{-3}$  and  
131  $265.2 \pm 157.1 \mu\text{g}\cdot\text{m}^{-3}$ , indicative of the high level of aerosol pollution. The average  
132 mass ratios of  $PM_1/PM_{2.5}$  and  $PM_{2.5}/PM_{10}$  are  $0.56 \pm 0.16$  and  $0.64 \pm 0.15$ , respectively.  
133 As we can see in Figure 1(b), the mass ratio of  $PM_1/PM_{2.5}$  is higher than that of  
134  $PM_{2.5}/PM_{10}$  before January 28, indicating that  $PM_1$  dominated the total mass. The  
135 aerosol concentration increased gradually and reached the maximum values at 12:00 of  
136 January 29, with  $PM_1$ ,  $PM_{2.5}$  and  $PM_{10}$  values of  $243.1 \mu\text{g}\cdot\text{m}^{-3}$ ,  $504.6 \mu\text{g}\cdot\text{m}^{-3}$  and  
137  $620.8 \mu\text{g}\cdot\text{m}^{-3}$ . The detailed interpretations of the high values will be presented in  
138 following section. Thereafter, the aerosol concentrations decreased rapidly to a lower  
139 level. The mass ratios of  $PM_1/PM_{2.5}$  and  $PM_{2.5}/PM_{10}$  showed opposite pattern with  
140 time variation during the period, indicating a decreasing fraction of  $PM_1$  compared  
141 with  $PM_{2.5}$  and an increasing fraction of  $PM_{2.5}$  compared with  $PM_{10}$  with increasing  
142 aerosol pollution. It is worth noting that the increase of  $PM_{1-2.5}$  was greatest during the  
143 period January 28 to 29, as showed in Figure 1(a). Figure S1 displays meteorological  
144 parameters during the episode. During this period, the average wind speed was 2.5  
145 m/s. Figure S2 shows an overview of wind rose of the local wind and the wind is  
146 mainly in the southerly and northerly quadrant, which can bring relative dirty or clean  
147 air masses, respectively. Figure 2 exhibits 72 hours backward trajectories of air  
148 parcels every 3 hours using Hysplit model from a height of 100m, with a total of six  
149 clusters yielded (<http://ready.arl.noaa.gov/HYSPLIT.php>). We should clarify that the  
150 southern area of Beijing often suffers more polluted atmosphere than that in the  
northern  
151 area due to more cities and population. The clusters of 1 to 5 are from the  
~~northern~~northerly

152 direction, with clean air and high transport height. Furthermore, a long transport  
153 pathway  
154 within 72 hours implies that those air parcels have a higher transport speed compared  
155 with cluster 6. The cluster 6, from southern and local directions with a fraction of  
156 47%, has the highest frequency. The cluster has a short transport distance of nearly  
157 400 km, low transport height and speed, resulting in a sufficient loading of surface air  
158 pollutions compared with other clusters. We also present sounding data in Beijing  
159 from ~~university~~ University of Wyoming twice a day (<http://weather.uwyo.edu/upperair/>), as  
160 shown in  
161 Figure 3. These lines with different colors represent soundings curves during the  
162 observation period. It is worth noting that an inversion layer between 1000m to  
163 1500m exists after January 27<sup>th</sup>. Particularly at 08:00 of 28<sup>th</sup> (Beijing time), the lapse  
164 ratio-rate of temperature is nearly 0.6°/100m, which means-indicates a very stable  
165 synoptic  
166 condition. Combined with low wind speed shown in figure S1, the horizontal motion  
167 is also limited during the pollution episode.

### 165 3.2 Aerosol optical properties

166 The aerosol scattering coefficient ( $\sigma_{sp}$ ) and backscattering coefficient ( $\sigma_{bsp}$ ) can be  
167 directly measured by the nephelometer and then aerosol backscattering fraction ( $b_{\lambda}$ ),  
168 scattering Ångström exponent ( $\text{Å}_{sp}$ ) and asymmetry parameter ( $g_{\lambda}$ ) can be calculated  
169 from the scattering coefficients, which have rarely been reported in Beijing using  
170 in-situ measurements. The aerosol light scattering coefficients show the same pattern  
171 as mass concentration of PM, as shown in Figure 4. Table 1 shows the statistics of the  
172 aerosol optical properties during this haze episode, and the average aerosol scattering

173 coefficients  $\sigma_{sp}^{450}$ ,  $\sigma_{sp}^{550}$  and  $\sigma_{sp}^{700}$  are  $1088.5 \pm 748.1 \text{ Mm}^{-1}$ ,  $877.2 \text{ Mm}^{-1} \pm 624.2 \text{ Mm}^{-1}$

174 and  $718.4 \text{ Mm}^{-1} \pm 530.8 \text{ Mm}^{-1}$ , respectively. After converting the aerosol light  
 175 scattering coefficients at 550nm to that of 525nm, the average  $\sigma_{sp}$  at 525nm are 3.2  
 176 times greater than the yearly average values at another site in Beijing, reported by He  
 177 et al. (2009). The average aerosol backscattering coefficients  $\sigma_{bsp}^{450}$ ,  $\sigma_{bsp}^{550}$  and  $\sigma_{bsp}^{700}$  are  
 178  $134.4 \text{ Mm}^{-1} \pm 87.1 \text{ Mm}^{-1}$ ,  $108.1 \text{ Mm}^{-1} \pm 71.1 \text{ Mm}^{-1}$  and  $98.7 \text{ Mm}^{-1} \pm 66.5 \text{ Mm}^{-1}$ ,  
 179 respectively, as presented in Figure 4 (b). During the whole campaign,  $\sigma_{sp}$  and  $\sigma_{bsp}$   
 180 at three wavelengths were highly correlated. Both  $\sigma_{sp}$  and  $\sigma_{bsp}$  increase gradually  
 181 from 24 to 29 January and decrease sharply to lower levels, which are consistent with  
 182 the variations of aerosol mass concentrations.

183 The backscattering ratio, which is also called the hemispheric backscatter fraction, is  
 184 the ratio of light scattered in the backward hemisphere to the total light scattered by  
 185 particles. It is related to particle size distribution and can be calculated as following;

$$186 \quad b_{\lambda} = \frac{\sigma_{bsp}^{\lambda}}{\sigma_{sp}^{\lambda}} \quad (1)$$

187 The average  $b_{\lambda}$  at three wavelengths are  $0.13 \pm 0.02$ ,  $0.14 \pm 0.02$  and  $0.15 \pm 0.02$ ,  
 188 respectively. A higher value of  $b_{\lambda}$  at 700nm indicates relatively more small size  
 189 particles that scatter light in the backward hemisphere. The scattering Ångström  
 190 exponent ( $\text{Å}_{sp}$ ) represents the wavelength dependence of scattering coefficient and is  
 191 related to the slope of the number-size distribution or the mean size and relative  
 192 concentrations of the accumulation and coarse mode aerosol. It is calculated using any  
 193 two of three channels as following;

$$194 \quad \text{Å} = - \frac{\log(\sigma^{\lambda_1}) - \log(\sigma^{\lambda_2})}{\log(\lambda_1) - \log(\lambda_2)} \quad (2)$$

195 The average  $\overset{0}{A}_{450/550}$  and  $\overset{0}{A}_{550/700}$  are  $1.2\pm 0.3$  and  $0.94\pm 0.3$ , respectively. The average  
 196  $\overset{0}{A}_{450/700}$  is  $1.1\pm 0.3$ , which is smaller than that of 1.46 in Guangzhou (Garland et al.,  
 197 2008) and 1.7 in Spain reported by (Titos et al., 2012), which indicates a more  
 198 dominant coarse mode particle compared with the other locations.

199 The asymmetry parameter  $g$  is a fundamental parameter for radiative transfer  
 200 calculation, and is defined as the intensity-weighted averaged cosine of the scattering  
 201 angle:

$$202 \quad g_{\lambda} = \frac{1}{2} \int_0^{\pi} \cos\theta P(\theta) \sin\theta d\theta \quad (3)$$

203 Where  $\theta$  is the angle between incident light and scattering direction and  $P(\theta)$  is the  
 204 angular distribution of scattered light (the phase function). The value of  $g_{\lambda}$  ranges  
 205 between -1 for completely backscattered light to +1 for completely forward scattered  
 206 light. Because there is no measurements method that can be directly obtained the  
 values of  $g$ , a fit

207 equation applied by Andrews et al. (2006) was used as in equation 4.

$$208 \quad g_{\lambda} = -7.143889*b_{\lambda}^3 + 7.464439*b_{\lambda}^2 - 3.9356*b_{\lambda} + 0.9893 \quad (4)$$

209 The average value of  $g_{\lambda}$  at 450nm, 550nm and 700nm are  $0.58\pm 0.04$ ,  $0.59\pm 0.05$  and  
 210  $0.54\pm 0.05$ , respectively. The three parameters of  $b_{\lambda}$ ,  $\overset{\circ}{A}_{sp}$  and  $g_{\lambda}$  can show a relative  
 211 contribution of particle size to light scattering. During 24 and 25 January,  $b_{\lambda}$  and  $\overset{\circ}{A}_{sp}$   
 212 shows higher values, which shows lower ones, as showed in Figure 4. However, the  
 213 opposite feature occurs when the haze developed. Especially during the highest  
 214 pollution periods (from 28 to 30 January), higher values of  $b_{\lambda}$ ,  $\overset{\circ}{A}_{sp}$  and lower values of  
 215  $g_{\lambda}$  appear, which indicates an increasing fraction of relative coarse aerosol, consistent  
 216 with the variation pattern of  $PM_1/PM_{2.5}$  showed in Figure 1(b).

### 217 3.3 particle number size distribution

218 The particle number-size distribution from January 25 to 31 is shown in Figure 5(a).  
219 The particle number concentration peaks at a diameter of around 100 nm. These  
220 particles are mainly from direct emissions of vehicles, cooking and new particle  
221 formation (Shi et al., 2001). Particle volume concentration and mass concentration are  
222 shown in figure 5(b) and (c), respectively, assuming an average aerosol bulk density  
223 of  $1.5 \text{ g.cm}^3$  and that all particles are regular spheres based on the research by (Zhang et  
224 al., 2004) in Pittsburgh PA, USA. The coarse mode particles between diameters of  
225 1000nm to 2500nm increased significantly during the most heavily pollution periods  
226 (28 and 29 January), as shown in Figure 5 (b) and 5 (c), which is consistent with  
227 interpretations of variation ratio of  $\text{PM}_{10}/\text{PM}_{2.5}$ . The time series of calculated mass  
228 concentration of  $\text{PM}_{2.5}$ , number concentrations of nucleation mode (14nm-25nm),  
229 Aitken mode (25nm-100nm), accumulation mode (100nm-1000nm) and coarse mode  
230 (1000 nm-2500nm) are presented in Figure 6. The calculated mass concentration of  
231  $\text{PM}_{2.5}$  matches well with measured values, with  $R^2$  values of 0.97, as shown in Figure  
232 S3. The nucleation mode particles show the highest number concentration during the  
233 period, with an average value greater than  $1.5 \times 10^6 \text{ cm}^{-3}$ , indicating large emission of  
234 reactive or low volatility, aerosol precursor gases (e.g. sulfur dioxide and organic  
235 vapors). The lowest particle number concentration is in coarse mode ( $D_m > 1000\text{nm}$ ),  
236 with an average value of  $3.18 \times 10^3 \text{ cm}^{-3}$ . The Aitken mode and accumulation mode  
237 also show high number concentrations, with the average values of  $1.90 \times 10^5 \text{ cm}^{-3}$  and  
238  $1.01 \times 10^6 \text{ cm}^{-3}$ . Compared with three years of measurements of particle number

239 concentration at another urban site in Beijing, the number concentrations of  
240 nucleation, Aitken and accumulation mode during this haze episode are more than 170  
241 times, 10 times and 120 times, respectively (Hu et al., 2009). The nucleation mode  
242 and Aitken mode particle show a significant increase at mid-day on 28 January, while  
243 the accumulation mode is not significant. This may be ascribed to the emissions from  
244 vehicle and cooking nearby our sampling site. It is worth noting that the concentration  
245 of coarse mode particle was highest on the 28th and 29th of January, which is  
246 consistent with the pattern of  $PM_{2.5}/PM_{10}$ . After the coagulation, condensation and  
247 hygroscopic growth, the number concentrations of nucleation mode and Aitken mode  
248 particle decrease on 12:00 of 30 January, as shown in Figure 6.

### 249 **3.4 aerosol chemical properties**

250 The time series of chemical compositions, mass fractions, O:C ratio and m/z 44 of  
251 NR- $PM_1$  are presented in Figure 7(a), (b) and (c). The average mass concentrations of  
252 organic, sulfate, nitrate, ammonium and chloride are  $62.1 \pm 46.1 \mu\text{g}\cdot\text{m}^{-3}$ ,  
253  $28.4 \pm 22.1 \mu\text{g}\cdot\text{m}^{-3}$ ,  $37.2 \pm 30.6 \mu\text{g}\cdot\text{m}^{-3}$ ,  $17.4 \pm 12.7 \mu\text{g}\cdot\text{m}^{-3}$  and  $5.5 \pm 4.2 \mu\text{g}\cdot\text{m}^{-3}$ , respectively.

254 The organic component is dominant in NR-  $PM_1$ , with an average mass fraction of  
255  $44.9\% \pm 11.7\%$ . Sulfate and nitrate species concentrations are also very high during the  
256 heavy haze event.

257 AMS enables the real time determination of size-resolved chemical compositions of  
258 different modes of particles as a function of time. Figure 8 shows the temporal  
variations

259 of the size distributions of the organic (a), sulfate (b), nitrate (c), ammonium (d) and  
260 chloride (e). The organic and chloride containing particles display a slightly broader

261 distribution than the other three species. All the aerosol components mainly reside in  
262 the accumulation mode with vacuum aerodynamic diameters around 700nm. Note that  
263 the AMS size distributions here are shown as a function of vacuum aerodynamic  
264 diameter,  $D_{va}$ , which is the aerodynamic diameter measured under free-molecular  
265 regime flow conditions. ~~For~~To a first approximation, 700nm in  $D_{va}$  corresponds  
266 roughly  
267 to 470 nm in physical diameter ~~of~~for spherical particles. It is worth noting that  
268 particles  
269 with optical diameters between 100nm and 1000nm have the highest scattering  
270 efficiency in the visible range (Liou, 2002), so a high concentration at this optimum  
271 aerosol size will lead to strong light scattering and ~~worse~~reduced visibility during the  
272 period.

270 These five aerosol components all show high concentrations from the afternoon of  
271 28 January to noon of 29 January, corresponding with the highest mass loading and  
272 light scattering of the whole pollution period. The detailed behaviors of particle  
273 number concentration, size-resolved organic, sulfate, nitrate, ammonium and particle  
274 mass concentration on January 28 are presented in Figure S5 and S6. The particle  
275 number concentrations show a burst at nearly 12:00, with  $D_m$  less than 100nm.  
276 Observations by Sakurai et al. (2005) in Atlanta, GA, USA recognized this as a plume  
277 related to a new particle formation event, which was accompanied by advection of  
278 local emissions. However, an increasing concentration of aerosol chemical  
279 components at about 11:00 on 28 January is observed by the AMS as shown in Figure  
280 S5.

280 The mass concentrations mainly reside on between 300nm and 1000nm in vacuum  
281 diameter. This may be due to the accumulation of air pollutants under-in the



~~stagnation~~stagnant

282 boundary layer. As we can see in figure S1, the meteorological parameters are

283 characterized by calm wind, low RH and increasing temperature in the morning,  
284 which leads to a stable boundary layer. Then, with increasing surface temperature and  
285 PBL height, the dilution causes the aerosol concentration decreasing in the afternoon.  
286 The concentrations of sulfate, ammonium and nitrate show an increasing trend from  
287 18:00. The major reasons are: (1) Increasing RH may enhance the heterogeneous  
288 reaction of SO<sub>2</sub> and NH<sub>3</sub> to produce sulfate and nitrate. (2) Decreased PBL height at  
289 night leads to accumulation of air pollutant. (3) Conversion of N<sub>2</sub>O<sub>5</sub> to nitrate via  
290 heterogenous or homogenous ways and reaction of OH and NO<sub>2</sub> (Kim et al., 2014).  
291 All of the above aspects result in the mass concentrations of nitrate and ammonium  
292 ~~have~~ having a distinct growth of particles with diameters between 100nm and 500nm  
on 28  
293 January.

### 294 **3.5 Increased formation of Secondary Organic Aerosol (SOA) during haze** 295 **pollution episode**

296 Figure 10 shows the variations of signal of m/z 44 as a function of organic  
297 aerosol mass concentration and the influence of relative humidity. The frequency  
298 distributions of organic mass and m/z 44 during the period are presented as well.

299 The ~~highest-greatest~~ frequency of occurrence of organic aerosol concentration  
appears ~~nearly~~ between mass concentrations of

300 20 to 35 μg·m<sup>-3</sup>, corresponding with signal fraction of m/z 44 less than 2. The  
301 signal of m/z 44 shows an increasing trend with increasing organic mass. The  
302 lower concentration of organic component mainly exists at RH below 40%,  
303 which is indicative of a relatively clean atmosphere in urban Beijing. It is

| 304

notable that the higher levels of the organic component occurs under high RH

305 conditions, ~~of which~~when aerosol water uptake ability is enhanced and the more  
306 highly hydrated particles are able to capture more water-soluble volatile organic  
307 compounds (VOCs). In this way, the dry mass concentration of organic aerosol  
308 increases after the water evaporated in the AMS. The studies of Ge et al. (2012)  
309 in central valley of California and Dall'Osto et al. (2009) in London also showed  
310 that aqueous-phase processes are responsible for the production of secondary  
311 organic aerosol species, most significantly during fog events.

### 312 **3.6 Light scattering apportionment**

313 Light scattering by atmospheric aerosols is highly dependent on their size,  
314 morphology and compositions (Liou, 2002). Sulfate, nitrate, ammonium and organic  
315 components in aerosol contribute most to light scattering, and particularly for  
316 diameters ranging from 100nm to 1000nm, they have the greatest light extinction  
317 efficiency (Seinfeld and Pandis, 1998). Here, a modified IMPROVE algorithm was  
318 employed to apportion light scattering coefficients at  $\lambda=550\text{nm}$  (Pitchford et al., 2007).  
319 The IMPROVE algorithm was based on a multiple liner regression method (Chan et  
320 al., 1999), which considers the degree to which aerosol light scattering is related to  
321 the mass concentration of each component combined with water uptake of inorganic  
322 component. The detailed introduction of the method can be can be found in  
323 Lowenthal et al. (1995).The  $f(\text{RH})$  curve obtained by Chen et al. (2014) during  
324 January in Northern China Plain is used here.

325 In our light apportionment calculation, the mass concentrations of ammonium sulfate,  
326 ammonium bisulfate, ammonium nitrate, ammonium chloride and organic were

327 required. However, the AMS can only provide us with mass concentrations of sulfate,  
328 nitrate, ammonium chloride and organic compounds. Here, a commonly accepted ion  
329 pairing scheme of calculating the neutral aerosol from the molar number of all ions  
330 simplified by Gysel et al. (2007) is applied. In this scheme, by setting the fraction of  
331 nitric acid to zero, the molar fraction of ammonium nitrate is equal to the molar  
332 fraction of nitrate ions. The rest of ammonium ions are assigned to ammonium  
333 bisulfate, ammonium sulfate and ammonium chloride according to ammonium molar  
334 fraction.

335 In the IMPROVE algorithm, the light scattering growth due to inorganic components  
336 were considered, while the contribution from organic aerosol did not take into account.  
337 Then, using the highly resolution mass concentrations of sulfate containing aerosol,  
338 ammonium nitrate, ammonium chloride and organic in submicron aerosol and aerosol  
339 scattering growth curve, we get-calculate a relationship of scattering coefficient and  
aerosol  
340 components and light scattering growth factor as showed in formula 9 . The fitting  
341 was finished-computed with under-MATLAB software (MATLAB R2010a). Figure 11  
(a) shows the  
342 time series of apportioned light scattering coefficients of each of the aerosol  
components  
343 compared with measured values during observation period. At the beginning of the  
344 periods, organic components dominated light scattering. With the development of the  
345 haze, the contribution of inorganic components increased as shown in Figure 11 (b).  
346 The total average light scattering contribution of each aerosol component is presented  
347 in Figure 12. The apportionment contributions from organic, sulfate, ammonium

348 nitrate and ammonium chloride were 54%, 24%, 12% and 10%, respectively, which

349 indicated the dominant contribution of organic and sulfate compounds to light  
350 scattering during this haze episode in Beijing. One should note that the apportioned  
351 light scattering coefficient using the IMPROVE method is highly related with its mass  
352 concentration, and organic aerosol has is a large mass-fractions of the mass-in-it. Yao et  
al. (2010)  
353 showed that the organic components contributed greatly to the light extinction (about  
354 45% contribution) by using AMS data during winter in Shenzhen, PRC. Watson (2002)  
355 also found the organic aerosol dominated light extinction in some cities, with  
356 fractions of 9%~50% in east USA.

$$\sigma_{sp}^{550} = 6.5 f(RH)[(NH_4)_2SO_4] + 6.5 f(RH)[NH_4HSO_4] + 2.2 f(RH)[NH_4NO_3] + 4.3 f(RH)[NH_4Cl] + 5.7[organic] + 57.3 \quad (9)$$

#### 358 **4. Summary and Conclusion**

359 Based on in-situ measurements, the physical and chemical properties of aerosol  
360 particles were characterized during a severe haze episode in Beijing from 24 January  
361 to 31 January during, 2013. The average mass concentrations of PM<sub>1</sub>, PM<sub>2.5</sub> and PM<sub>10</sub>  
362 were 99.1±67.1 μg·m<sup>-3</sup>, 188.3±128.8 μg·m<sup>-3</sup> and 265.2±157.1 μg·m<sup>-3</sup>, respectively, and  
363 an increasing fraction of PM<sub>1-2.5</sub> was significant during the most heavy pollution  
364 periods. The averaged scattering coefficient at 550 nm was 877.2 Mm<sup>-1</sup>±624.2 Mm<sup>-1</sup>,  
365 and an increasing amount of relative coarse particle also can be seen from the  
366 variations of backscattering ratios, asymmetry parameter and scattering Ångström  
367 exponent. Particle number size distribution (14 nm to 2500nm) showed high number  
368 concentrations in the nucleation and accumulation modes. Size-resolved chemical  
369 composition of submicron aerosol from a HR-ToF-AMS showed that the mass

| 370 concentration of organic, sulfate, nitrate, ammonium and chlorine mainly resided on



371 500nm-800nm in vacuum diameter, and sulfate and ammonium contributed to the  
372 growth of particle during the most heavily polluted day on January 28.  
373 High emissions of regional background pollutants combined with stable synoptic  
374 conditions  
375 and increasing of relative humidity, which lead to enhanced water uptake ability of  
376 submicron aerosol and formation of secondary aerosol, may be the main reasons for  
377 the heavy haze episode. Light scattering apportionment showed that organic, sulfate  
378 containing components, ammonium nitrate and ammonium chloride contributed to  
379 light scattering fractions of 54%, 24%, 12% and 10%, respectively. Considering their  
380 dominant fractional contribution to light scattering and light extinction, our study  
381 indicated that organic components also played an important role in visibility  
382 degradation  
383 during the winter haze episode in Beijing.

### 382 **Acknowledgment**

383 We acknowledge Professor Zhang Wu of Lanzhou University for help in nephelometer  
384 maintaining maintenance. We also acknowledge NOAA, university and University of  
385 Wyoming for backward  
386 trajectory calculations soft and meteorological upper air data analysis, respectively. This  
387 work was supported  
388 by National Natural Science Foundation of China (41230642), the CAS Strategic  
389 Priority Research Program grant XDA05100100 and XDB05020402.

### 388 **Reference**

389 Anderson, T.L. et al., 2003. Atmospheric science. Climate forcing by aerosol--a hazy picture. Science,  
390 300(5622): 1103-4.  
391 Anderson, T. L., and Ogren, J. A.: Determining Aerosol Radiative Properties Using  
392 the Tsi 3563 Integrating Nephelometer, Aerosol Science and Technology, 29, 57-



394 Andrews, E. et al., 2006. Comparison of methods for deriving aerosol asymmetry parameter. *Journal of*  
395 *Geophysical Research*, 111(D5).

396 Beddows, D.C.S., Dall'osto, M. and Harrison, R.M., 2010. An Enhanced Procedure for the Merging of  
397 Atmospheric Particle Size Distribution Data Measured Using Electrical Mobility and  
398 Time-of-Flight Analysers. *Aerosol Science and Technology*, 44(11): 930-938.

399 Chan, Y.C. et al., 1999. Source apportionment of visibility degradation problems in Brisbane (Australia)  
400 using the multiple linear regression techniques. *Atmospheric Environment*, 33(19):  
401 3237-3250.

402 Chen, J. et al., 2012. A parameterization of low visibilities for hazy days in the North China Plain.  
403 *Atmospheric Chemistry and Physics*, 12(11): 4935-4950.

404 Chen, J., Zhao, C.S., Ma, N. and Yan, P., 2014. Aerosol hygroscopicity parameter derived from the  
405 light scattering enhancement factor measurements in the North China Plain. *Atmos. Chem.*  
406 *Phys.*, 14(15): 8105-8118.

407 Cheng, Y.F. et al., 2012. Size-resolved measurement of the mixing state of soot in the megacity Beijing,  
408 China: diurnal cycle, aging and parameterization. *Atmospheric Chemistry and Physics*, 12(10):  
409 4477-4491.

410 Dall'Osto, M., Harrison, R.M., Coe, H. and Williams, P., 2009. Real-time secondary aerosol formation  
411 during a fog event in London. *Atmos. Chem. Phys.*, 9(7): 2459-2469.

412 Deng, Z.Z. et al., 2013. Examination of parameterizations for CCN number concentrations based on  
413 in-situ aerosol activation property measurements in the North China Plain. *Atmospheric*  
414 *Chemistry and Physics Discussions*, 13(1): 145-176.

415 Garland, R.M. et al., 2008. Aerosol optical properties in a rural environment near the mega-city  
416 Guangzhou, China: implications for regional air pollution, radiative forcing and remote  
417 sensing. *Atmos. Chem. Phys.*, 8(17): 5161-5186.

418 Ge, X., Zhang, Q., Sun, Y., Ruehl, C.R. and Setyan, A., 2012. Effect of aqueous-phase processing on  
419 aerosol chemistry and size distributions in Fresno, California, during wintertime.  
420 *Environmental Chemistry*, 9(3): 221.

421 Gysel, M. et al., 2007. Closure study between chemical composition and hygroscopic growth of aerosol  
422 particles during TORCH2. *Atmos. Chem. Phys.*, 7(24): 6131-6144.

423 He, X. et al., 2009. An intensive study of aerosol optical properties in Beijing urban area. *Atmos. Chem.*  
424 *Phys.*, 9: 8903-8915

425 Hu, M., He, L., Huang, X. and Wu, Z.: Chemical and physical properties, source and  
426 formation of fine and ultrafine particle in Beijing, Science Press, 2009.

427 Huang, K. et al., 2010a. Relation between optical and chemical properties of dust aerosol over Beijing,  
428 China. *Journal of Geophysical Research*, 115.

429 Huang, X.F. et al., 2010b. Highly time-resolved chemical characterization of atmospheric submicron  
430 particles during 2008 Beijing Olympic Games using an Aerodyne High-Resolution Aerosol  
431 Mass Spectrometer. *Atmospheric Chemistry and Physics*, 10(18): 8933-8945.

432 Kaufman, Y.J., Koren, I., Remer, L.A., Rosenfeld, D. and Rudich, Y., 2005. The effect of smoke, dust,  
433 and pollution aerosol on shallow cloud development over the Atlantic Ocean. *Proc Natl Acad*  
434 *Sci U S A*, 102(32): 11207-12.

435 Koren, I., Kaufman, Y.J., Rosenfeld, D., Remer, L.A. and Rudich, Y., 2005. Aerosol invigoration and

436 restructuring of Atlantic convective clouds. *Geophysical Research Letters*, 32(14): n/a-n/a.

437 Li, W.J., Shao, L.Y. and Buseck, P.R., 2010. Haze types in Beijing and the influence of agricultural  
438 biomass burning. *Atmospheric Chemistry and Physics*, 10(17): 8119-8130.

439 Liu, X.G. et al., 2013. Formation and evolution mechanism of regional haze: a case study in the  
440 megacity Beijing, China. *Atmospheric Chemistry and Physics*, 13(9): 4501-4514.

441 Liu, Z. et al., 2015. Seasonal and diurnal variation in particulate matter (PM<sub>10</sub> and PM<sub>2.5</sub>) at an urban  
442 site of Beijing: analyses from a 9-year study. *Environmental Science and Pollution Research*,  
443 22(1): 627-642.

444 Liu, Z.R., Hu, B., Liu, Q., Sun, Y. and Wang, Y.S., 2014. Source apportionment of urban fine particle  
445 number concentration during summertime in Beijing. *Atmospheric Environment*(0).

446 Lohmann, U. and Feichter, a.J., 2005. Global indirect aerosol effects: a review. *Atmos. Chem. Phys.*  
447 , 5: 715-737.

448 Liou, K.N.: *An introduction to atmospheric radiation (second edition)* , Elsevier  
449 Science, 2002.

450 Lowenthal, D.H., Rogers, C.F., Saxena, P., Watson, J.G. and Chow, J.C., 1995. Sensitivity of estimated  
451 light extinction coefficients to model assumptions and measurement errors. *Atmospheric*  
452 *Environment*, 29(7): 751-766.

453 Ma, N. et al., 2012. A new method to determine the mixing state of light absorbing carbonaceous using  
454 the measured aerosol optical properties and number size distributions. *Atmospheric Chemistry*  
455 *and Physics*, 12(5): 2381-2397.

456 Meier, J. et al., 2009. Hygroscopic growth of urban aerosol particles in Beijing (China)  
457 during wintertime: a comparison of three experimental methods. *Atmos. Chem. Phys.*, , 9: 6865–6880  
458

459 Nel, A., 2005. Atmosphere. Air pollution-related illness: effects of particles. *Science*, 308(5723): 804-6.

460 Pan, X.L. et al., 2009. Observational study of influence of aerosol hygroscopic growth on scattering  
461 coefficient over rural area near Beijing mega-city. *Atmos. Chem. Phys.*  
462 , 9: 7519–7530.

463 Pitchford, M. et al., 2007. Revised Algorithm for Estimating Light Extinction from IMPROVE Particle  
464 Speciation Data. *Journal of the Air & Waste Management Association*, 57(11): 1326-1336.

465 Poschl, U., 2005. Atmospheric aerosols: composition, transformation, climate and health effects.  
466 *Angew Chem Int Ed Engl*, 44(46): 7520-40.

467 Qu, W.J. et al., 2010. Spatial distribution and interannual variation of surface PM<sub>10</sub>  
468 concentrations over eighty-six Chinese cities. *Atmospheric Chemistry and Physics*, 10(12):  
469 5641-5662.

470 Quan, J. et al., 2011. Analysis of the formation of fog and haze in North China Plain (NCP).  
471 *Atmospheric Chemistry and Physics*, 11(15): 8205-8214.

472 Ramanathan, V., Crutzen, P.J., Kiehl, J.T. and Rosenfeld, D., 2001. Aerosols, climate, and the  
473 hydrological cycle. *Science*, 294(5549): 2119-24.

474 Sakurai, H. et al., 2005. Hygroscopicity and volatility of 4–10 nm particles during summertime  
475 atmospheric nucleation events in urban Atlanta. *Journal of Geophysical Research:*  
476 *Atmospheres*, 110(D22): D22S04.

477 Seinfeld, J. H., and Pandis, S. N.: *Atmospheric Chemistry and physics, From Air*

478 Pollution to Climate Changes, Wiley, New York, USA, 1998.

479 Shi, J.P., Evans, D.E., Khan, A.A. and Harrison, R.M., 2001. Sources and concentration of  
480 nanoparticles (<math>10\text{ nm}</math> diameter) in the urban atmosphere. *Atmospheric Environment*,  
481 35(7): 1193-1202.

482 Sun, Y.L., Zhuang, G.S., Tang, A., Wang, Y. and And An, Z., 2006. Chemical Characteristics of  
483 PM<sub>2.5</sub> and PM<sub>10</sub> in Haze-fog Episodes in Beijing. *Environ. Sci. Technol.*, 40: 3148-3155.

484 Tang, G. et al., 2012. Spatial-temporal variations in surface ozone in Northern China as observed  
485 during 2009–2010 and possible implications for future air quality control strategies. *Atmos.*  
486 *Chem. Phys.*, 12(5): 2757-2776.

487 Titos, G. et al., 2012. Optical properties and chemical composition of aerosol particles at an urban  
488 location: An estimation of the aerosol mass scattering and absorption efficiencies. *Journal of*  
489 *Geophysical Research: Atmospheres*, 117(D4): D04206.

490 Twomey, S., 1977. The Influence of Pollution on the Shortwave Albedo of Clouds. *Journal of the*  
491 *Atmospheric Sciences*, 34: 1149-1152.

492 Wang, K.C., Dickinson, R.E., Su, L. and Trenberth, K.E., 2012a. Contrasting trends of mass and optical  
493 properties of aerosols over the Northern Hemisphere from 1992 to 2011. *Atmospheric*  
494 *Chemistry and Physics*, 12(19): 9387-9398.

495 Wang, L. et al., 2012b. Understanding haze pollution over the southern Hebei area of China using the  
496 CMAQ model. *Atmospheric Environment*, 56: 69-79.

497 Wang, Y. et al., 2013. Mechanism for the formation of the January 2013 heavy haze pollution episode  
498 over central and eastern China. *Science China Earth Sciences*.

499 Wang, Y.H. et al., 2014. Ozone weekend effects in the Beijing–Tianjin–Hebei metropolitan area, China.  
500 *Atmos. Chem. Phys.*, 14(5): 2419-2429.

501 Watson, J.G., 2002. Visibility: Science and Regulation. *Journal of the Air & Waste Management*  
502 *Association*, 52(6): 628-713.

503 Wehner, B. et al., 2008. Relationships between submicrometer particulate air pollution and  
504 air mass history in Beijing, China, 2004–2006. *Atmos. Chem. Phys.*, 8: 6155–6168.

505 Wu, Z. et al., 2007. New particle formation in Beijing, China: Statistical analysis of a 1-year data set.  
506 *Journal of Geophysical Research*, 112(D9).

507 Yang, M., Howell, S.G., Zhuang, J. and Huebert, a.B.J., 2009. Attribution of aerosol light absorption to  
508 black carbon, brown  
509 carbon, and dust in China – interpretations of atmospheric  
510 measurements during EAST-AIRE. *Atmos. Chem. Phys.*, 9: 2035–2050.

511 Yao, T. et al., 2010. High time resolution observation and statistical analysis of atmospheric light  
512 extinction properties and the chemical speciation of fine particulates. *SCIENCE CHINA*  
513 *Chemistry*, 53(8): 1801-1808.

514 Zhang, J.K. et al., 2014. Characterization of submicron aerosols during a month of serious pollution in  
515 Beijing, 2013. *Atmos. Chem. Phys.*, 14(6): 2887-2903.

516 Zhang, Q., Quan, J., Tie, X., Huang, M. and Ma, X., 2011. Impact of aerosol particles on cloud  
517 formation: Aircraft measurements in China. *Atmospheric Environment*, 45(3): 665-672.

518 Zhang, Q. et al., 2004. Insights into the Chemistry of New Particle Formation and Growth Events in  
519 Pittsburgh Based on Aerosol Mass Spectrometry. *Environmental Science & Technology*,  
520 38(18): 4797-4809.

521 Zhang, Q.H., Zhang, J.P. and Xue, H.W., 2010. The challenge of improving visibility in Beijing.  
522 Atmospheric Chemistry and Physics, 10(16): 7821-7827.

523 Zhang, X. et al., 2013. Factors contributing to haze and fog in China. Chinese Science Bulletin  
524 (Chinese Version), 58(13): 1178.

525 Zhang, X.Y. et al., 2012. Atmospheric aerosol compositions in China: spatial/temporal variability,  
526 chemical signature, regional haze distribution and comparisons with global aerosols.  
527 Atmospheric Chemistry and Physics, 12(2): 779-799.

528 Zhao, X.J. et al., 2013. Analysis of a winter regional haze event and its formation mechanism in the  
529 North China Plain. Atmospheric Chemistry and Physics, 13(11): 5685-5696.

530

531

532

533

534

535

536

537

538

539

540

541

542

543

544

545

546

547

548

549 Table 1 The statistic of aerosol optical properties during observation period.

Parameter	mean	median	Standard derivation	5% quantile	95% quantile
$\sigma_{sp}^{450}$ (Mm <sup>-1</sup> )	1088.5	924.4	748.1	48.1	2386.3
$\sigma_{sp}^{550}$ (Mm <sup>-1</sup> )	877.2	748.4	624.2	36.6	1993.4
$\sigma_{sp}^{700}$ (Mm <sup>-1</sup> )	718.4	628.2	530.9	28.7	1703.3
$\sigma_{bsp}^{450}$ (Mm <sup>-1</sup> )	134.4	122.8	87.1	7.6	281.4
$\sigma_{bsp}^{550}$ (Mm <sup>-1</sup> )	108.1	96.4	71	6.1	228.5
$\sigma_{bsp}^{700}$ (Mm <sup>-1</sup> )	98.7	89.3	66.5	7.3	214.4
$b_{450}$	0.13	0.13	0.02	0.11	0.16
$b_{550}$	0.14	0.12	0.02	0.11	0.17
$b_{700}$	0.15	0.14	0.02	0.13	0.19
$A_{450/550}^0$	1.2	1.3	0.3	0.74	1.7
$A_{550/700}^0$	0.94	1.0	0.3	0.41	1.4
$g_{450}$	0.58	0.6	0.04	0.52	0.62
$g_{550}$	0.57	0.6	0.05	0.50	0.63
$g_{700}$	0.54	0.56	0.05	0.46	0.60

550

551

552 Table 2 The statistic of particle number concentration during observation period.

Parameter	Mean	median	Standard derivation	5% quantile	95% quantile
Nucleation(cm <sup>-3</sup> )	1.90×10 <sup>5</sup>	1.8×10 <sup>5</sup>	8.3×10 <sup>4</sup>	6.3×10 <sup>4</sup>	3.4×10 <sup>5</sup>
Aitken(cm <sup>-3</sup> )	1.5×10 <sup>6</sup>	1.4×10 <sup>6</sup>	6.4×10 <sup>5</sup>	5.7×10 <sup>5</sup>	2.7×10 <sup>6</sup>
Accumulation(cm <sup>-3</sup> )	1×10 <sup>6</sup>	9.9×10 <sup>6</sup>	3.9×10 <sup>5</sup>	4.7×10 <sup>5</sup>	1.6×10 <sup>6</sup>
Coarse (cm <sup>-3</sup> )	3.1×10 <sup>3</sup>	2.9×10 <sup>3</sup>	2.3×10 <sup>3</sup>	2.5×10 <sup>2</sup>	7.0×10 <sup>3</sup>

553

554

555

556

557

558

559

560

561

562

563

564

565

566

567



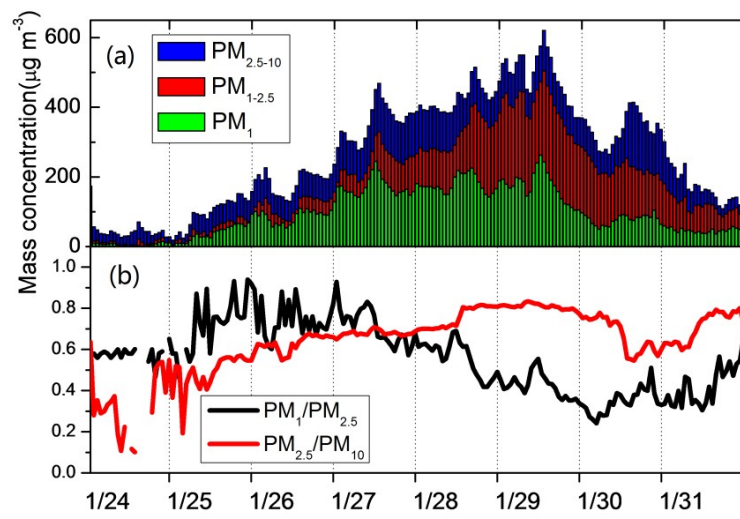


Figure 1 Time series of (a) mass concentrations of  $\text{PM}_1$ ,  $\text{PM}_{1-2.5}$  and  $\text{PM}_{2.5-10}$ , (b) mass ratios of  $\text{PM}_1/\text{PM}_{2.5}$  and  $\text{PM}_{2.5}/\text{PM}_{10}$

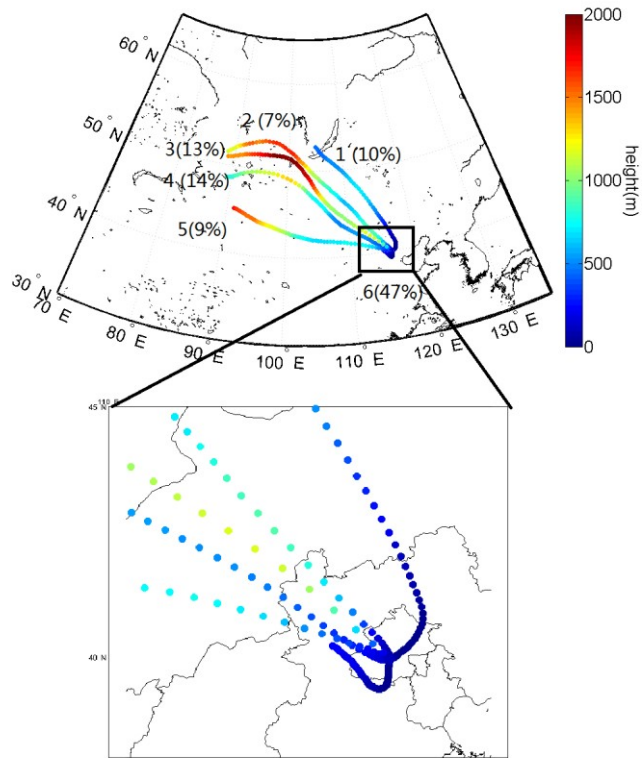


Figure 2 The three days backward trajectory of air parcels during the observation period; the colors of air trajectories represent height during transport.

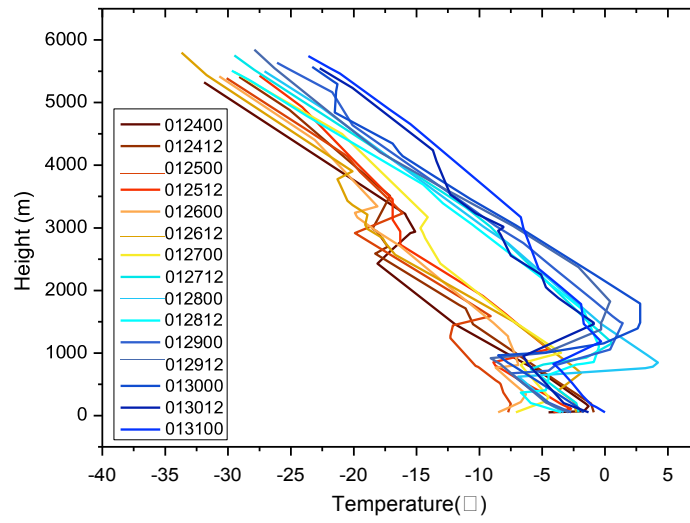


Figure 3 The temperature profiles during observation period. The legend stands for UTC time. For example, 012400 means 0:00 on January 24<sup>th</sup>.

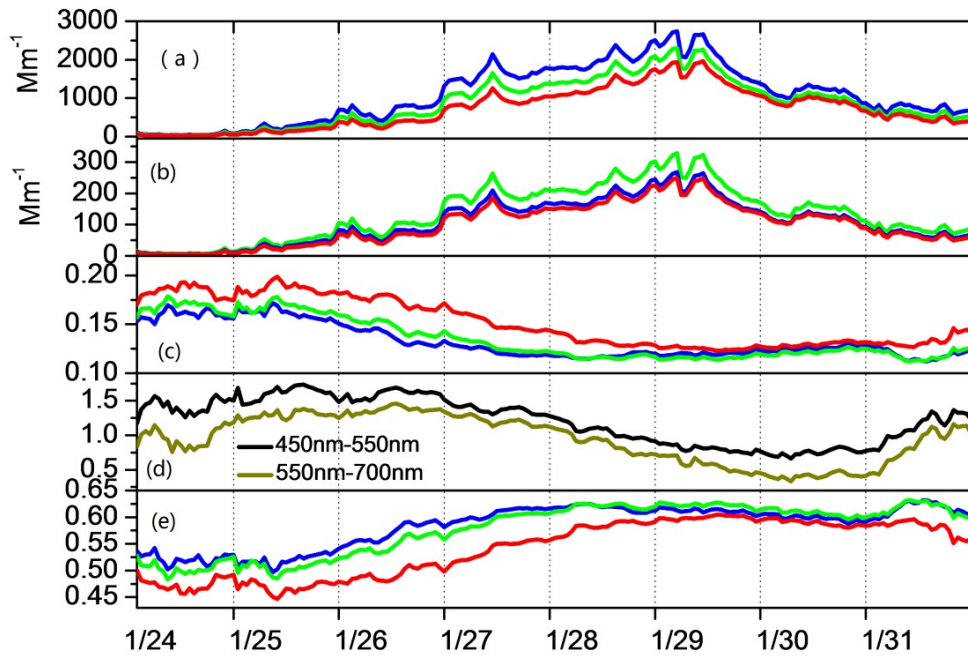


Figure 4 Time series of (a) scattering coefficients  $\sigma_{sp}$ , (b) backscattering coefficients  $\sigma_{bsp}$ , (c) backscattering ratios  $b_{\lambda}$ , (e) asymmetry parameter  $g_{\lambda}$  at wavelengths of 450nm (blue), 550nm (green) and 700nm (red) (d) scattering Ångström exponent ( $\text{\AA}_{sp}$ ) from 450nm-550nm (black) and 550nm-700nm(brown).

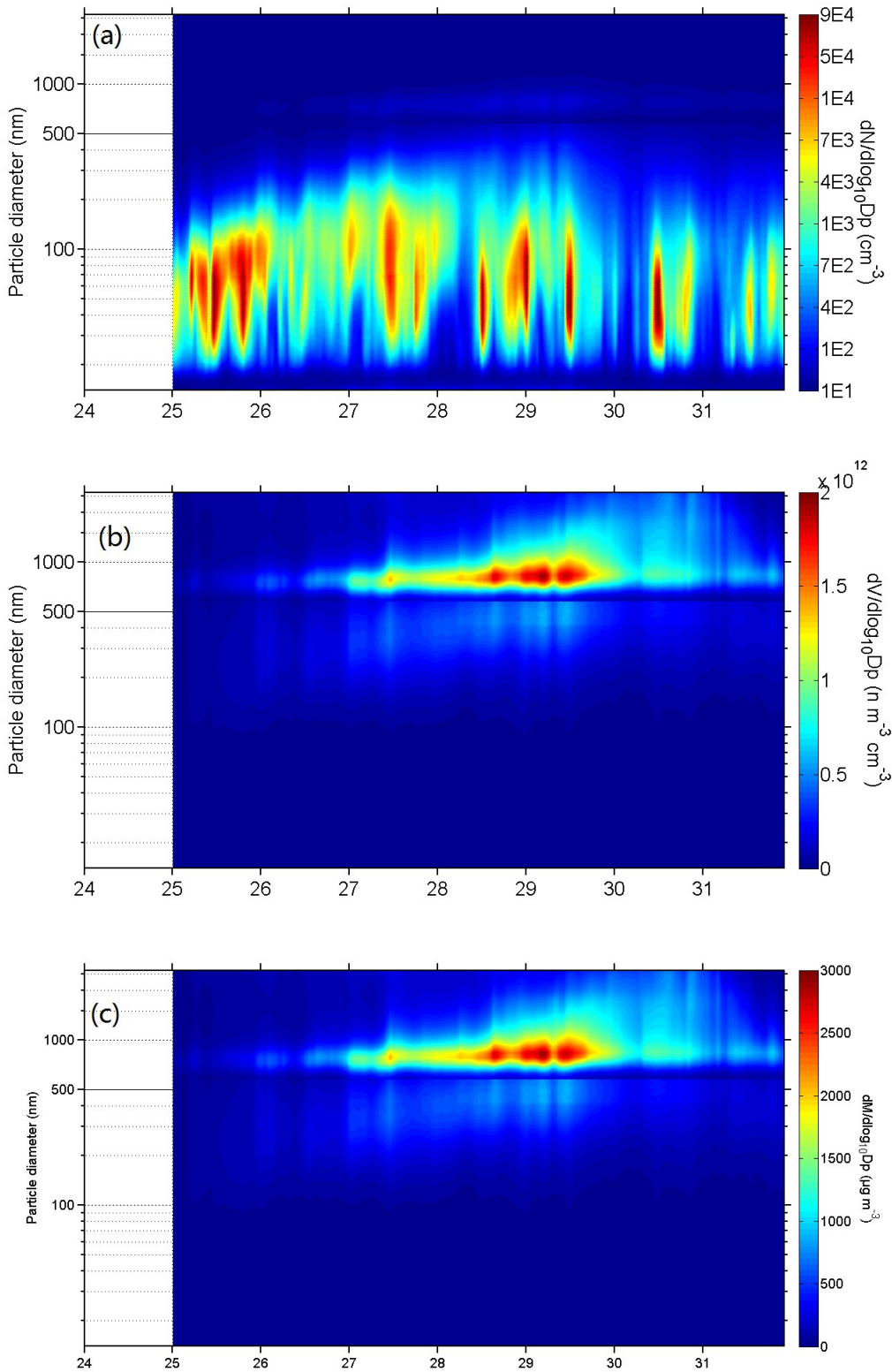


Figure 5 Time series of (a) particle number size distribution (b) particle volume size distribution (c) particle mass size distribution between 14.1nm-2458nm using SMPS combined with APS from January 25 to 31. The x-axis represents the data of January

and y-axis represents particle diameter (nm). The color in the figure 3 represents particle concentration ( $dN/d\log D_p$ ).

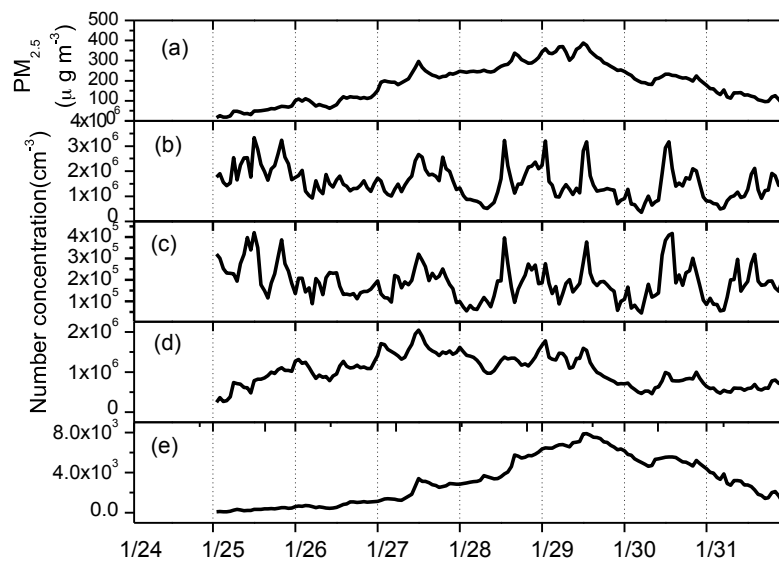


Figure 6 Time series of (a) particle mass concentration calculated from number size distribution and number concentrations of (b) nucleation mode (14.1nm-25nm), (c) Aitken mode (25nm-100nm), (d) accumulation mode (100nm-1000nm) and (e) coarse mode (1000nm-2458nm) from January 25 to January 31.

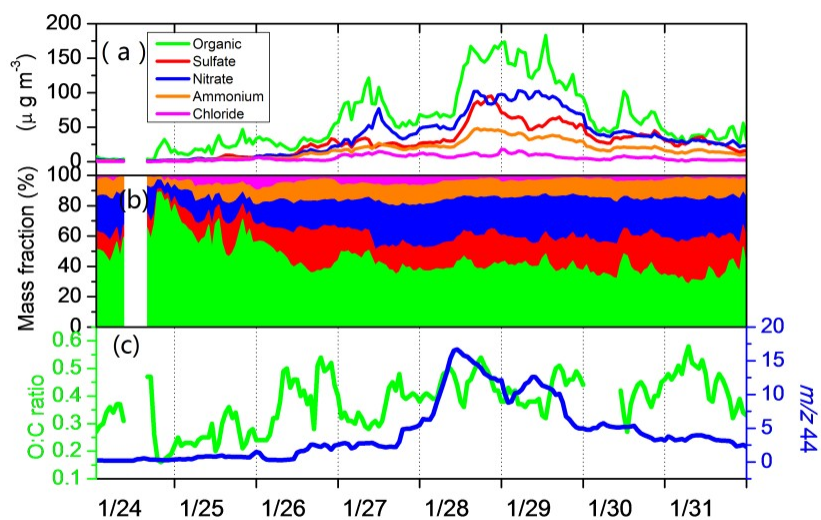
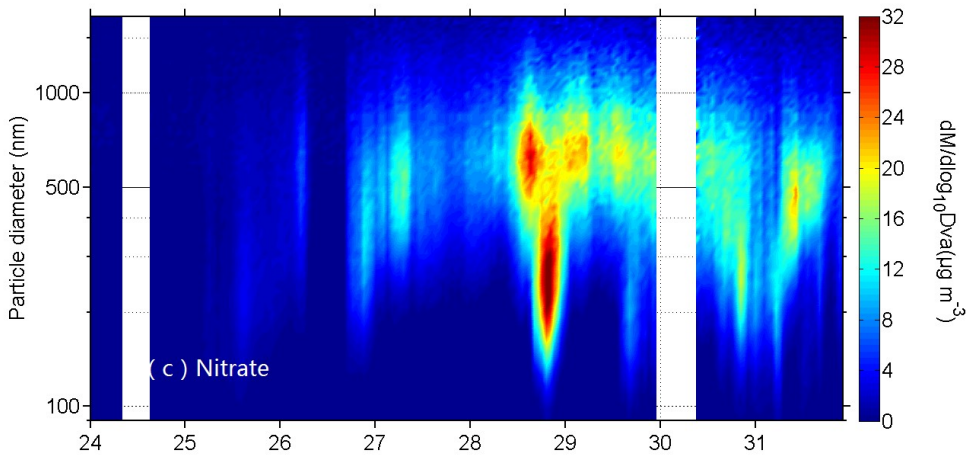
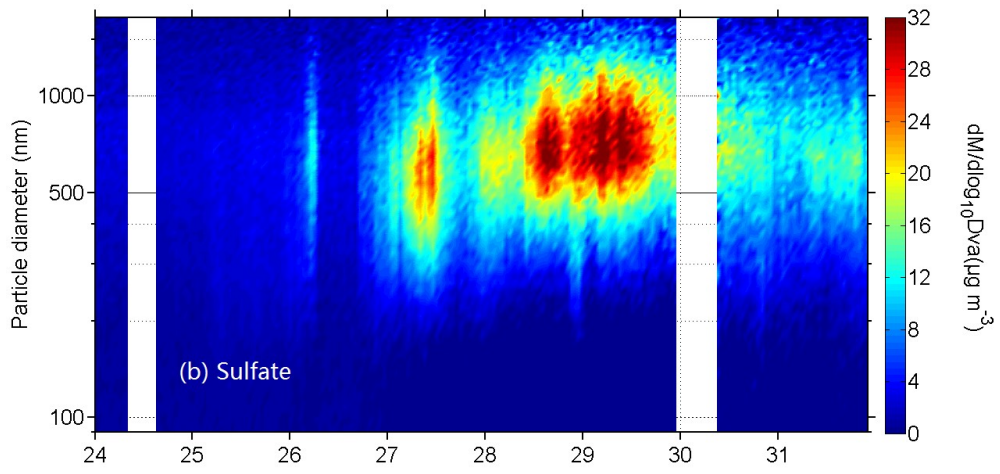
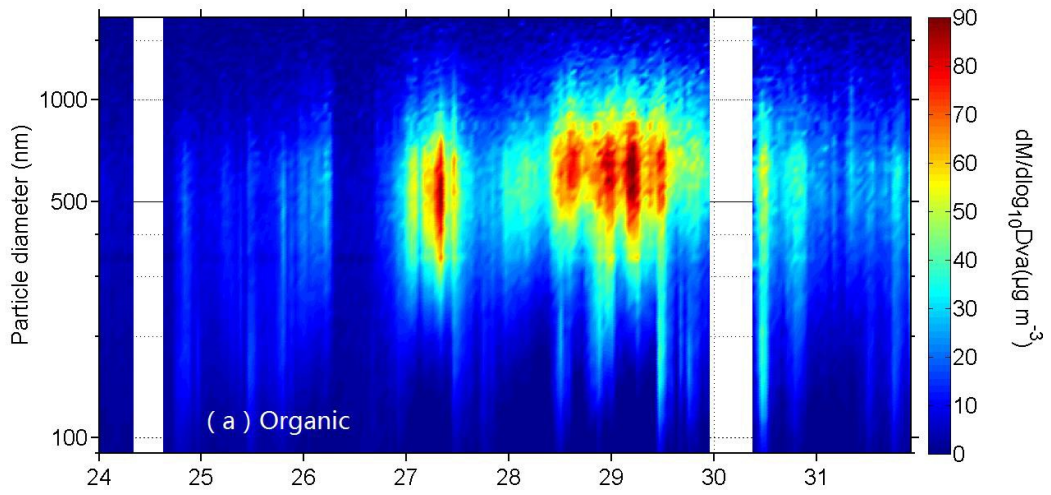


Figure 7 Time series of (a) mass concentrations of organic, sulfate, nitrate, ammonium and chloride in submicron aerosol (b) mass fractions of organic, sulfate, nitrate, and ammonium and chloride (c) O: C ratio and  $m/z$  44 during the haze episode.





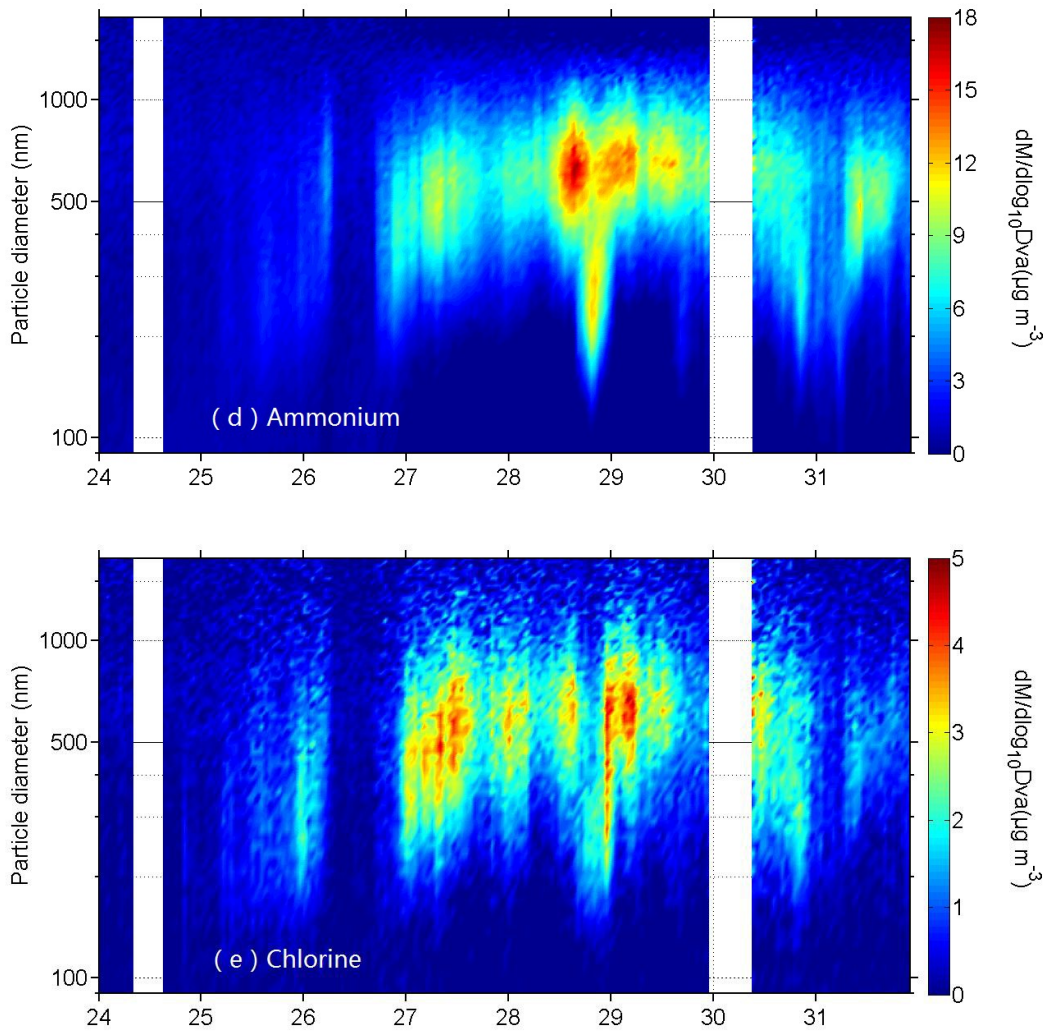


Figure 8 Size-resolved chemical compositions of (a) organic (b) sulfate (c) nitrate (d) ammonium and (e) chlorine

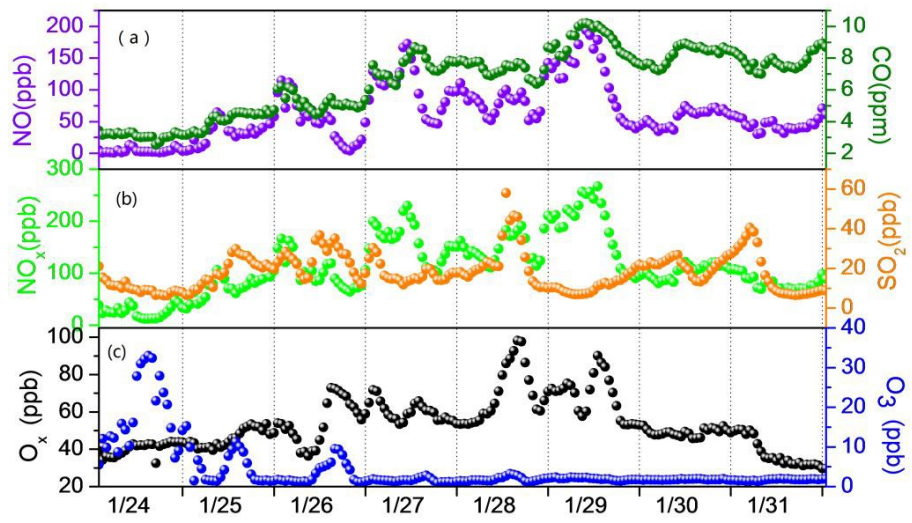


Figure 9 Mixing ratios of (a) NO and CO (b) NO<sub>x</sub> and SO<sub>2</sub> (c) O<sub>x</sub> and O<sub>3</sub>

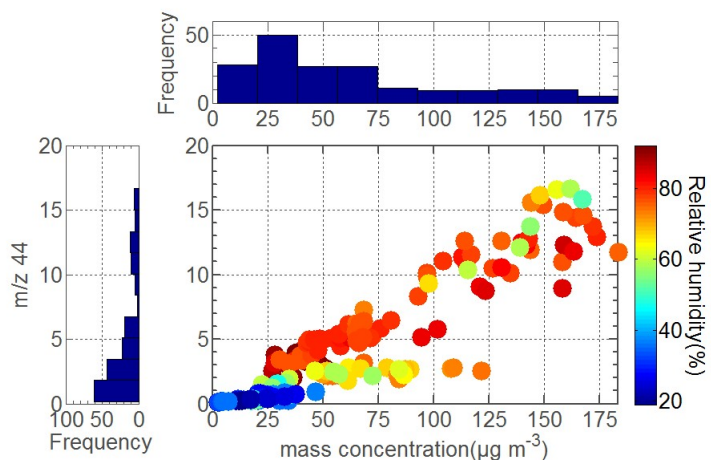


Figure 10 (left panel) the frequency distribution of m/z 44, (top panel) the frequency distribution of organic mass, (center panel) abundance of m/z 44 as a function of organic aerosol mass concentration and the influence of RH (left, color scale).

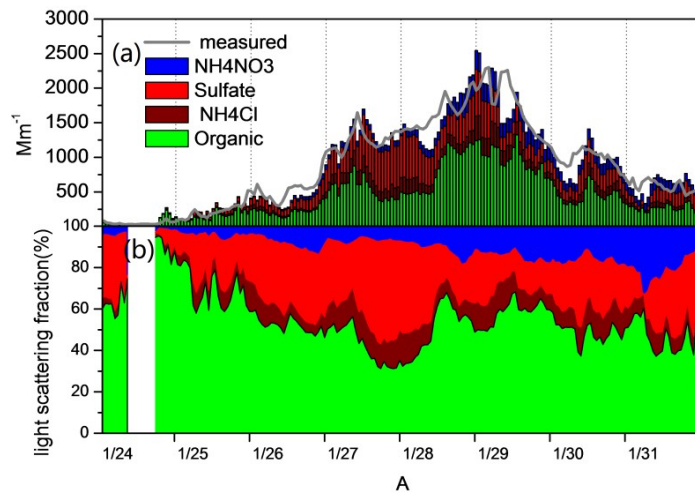


Figure 11 Time series of (a) apportioned light scattering coefficients of each aerosol components compared with measured (b) light scattering fractions of each aerosol components.

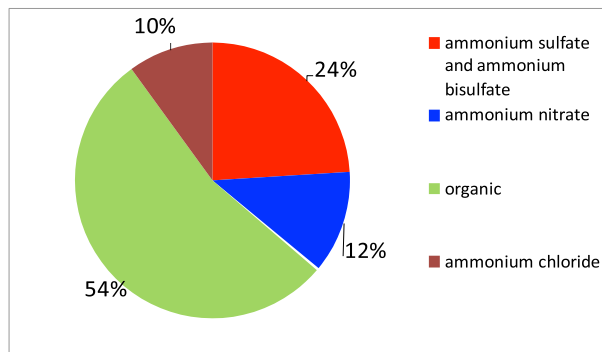


Figure 12 Averaged light scattering contribution of each aerosol components during the haze episode